IOP Publishing Phys. Scr. 97 (2022) 125008 https://doi.org/10.1088/1402-4896/ac9e7e

Physica Scripta

RECEIVED
7 September 2022

REVISED
13 October 2022

ACCEPTED FOR PUBLICATION
28 October 2022

PUBLISHED
10 November 2022

PAPER

Time-dependent finite-difference model for transient and steady-state analysis of thermoelectric bulk materials

R A Rathnayake [1,2], H Wijekoon [1,2], B M K Pemasiri [3] and N D Subasinghe [1,*]

[1] National Institute of Fundamental Studies, Hantana Road, Kandy, Sri Lanka
[2] Postgraduate Institute of Science, University of Peradeniya, Sri Lanka
[3] Department of Physics, Faculty of Science, University of Peradeniya, Sri Lanka
[*] Author to whom any correspondence should be addressed.

E-mail: deepal.su@nifs.ac.lk

Keywords: finite-difference methods, nonlinear PDE, numerical model, thermoelectricity, explicit-method

Abstract

A mathematical model of coupled thermoelectricity is presented to investigate the transient and steady-state behaviour of thermoelectric bulk material. Governing partial differential equations (PDEs) for the coupled thermal and electrical behaviour of the thermoelectric model are discretised using the explicit finite-difference method. Differencing schemes like Upwind and Lax–Wendroff methods are employed to obtain solutions for the first-order hyperbolic PDEs, whereas FTCS (Forward Time, Centred Space) scheme is employed to solve second-order parabolic PDEs. Courant-Friedrichs-Lewy and Von Neumann stability analyses are done to ensure the stability and convergence of the model. The model considers the temperature dependency of thermal conductivity, electrical conductivity, and *Seebeck* coefficient of the P/N materials separately. and accounts for the Seebeck, Peltier, and Joule-Thomson effects in thermoelectric materials. The new model is practically useful to predict the transient and steady-state behaviours of a thermoelectric device with multiple P-N elements. The results of the presented finite-difference model are proven to agree well with experimental values as well as 3D simulations with ANSYS®.

1. Introduction

Thermoelectricity is the direct conversion of thermal energy into electricity [1]. The thermoelectric effect, generally known as the Seebeck effect, was discovered about two centuries ago, but it became more popular over the last few decades, mainly as it can be utilized as a new way to recover waste heat energy into usable electricity, thus increasing the overall efficiency of numerous energy transformation processes [2]. A device, which utilizes the principle of the Seebeck effect is called a Thermoelectric Generator (TEG), which is a solid-state device composed of several couples of p- and n- types semiconductor elements.

Over the past decades, a large number of attempts have been made to increase the performance of the TEG devices. Most of the current research works [3–5] are concentrated on developing new thermoelectric materials to obtain a higher '*figure-of-merit*' (ZT) value, which determines the energy conversion efficiency of thermoelectric material. Usually, before assembling the actual physical module, the performance of a TEG device is often determined by using a computer model. According to the literature, three major types of modelling platforms can be found for thermoelectrics. The first type of model uses the equivalent circuit models to solve thermoelectric problems. Typically, these models have been developed using open-source, analogue-electronic circuit simulator software called SPICE [6–9]. The second type of models has been developed in multi-physics engineering simulation software like ANSYS® [10, 11], Cosmol [12], and Fluent [13]. Most of these commercial software cannot capture all the essential physics of the TE device, including Peltier, Thomson, Joule effects and take the temperature dependency material properties into account. Therefore, some models are confined by the limitations of the software packages. The best way to model un-modelled physics is to numerically solve the partial differential equations (PDEs) that describe the thermal and electrical characteristics

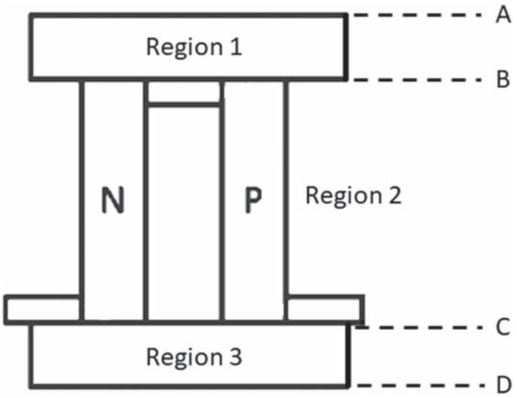

Figure 1. The geometry of the model. Region 1: hot-side substrate material, Region 2: P and N thermoelectric material, Region 3: cold-side substrate material. Letter A, B, C, D represent the boundary A, B, C, D, respectively.

of thermoelectric materials. So, the third type is the numerical models that have been created in programming platforms using a programming language [14–16].

In this work, a complete formulation and implementation of finite-difference method based thermoelectric model is presented. The model contains the system of PDEs for the typical TE module (figure 1): two heat equations (one for the hot side substrate and the other for the cold side substrate), pair of PDEs for both P and N type thermoelectric materials (one for the heat transport, the other for the electric field), set of boundary equations for boundaries A, B, C, and D. The main advantage of the proposed finite-difference model over the previous implementations [15] is that, in this formulation, electric field and heat transport in both P and N type materials are handled separately, and the temperature dependencies of thermal conductivity, electrical conductivity, and Seebeck coefficient of the P/N materials are addressed directly. PDEs, which are time-dependent, are discretised using the finite-difference 'explicit' method, which is particularly well-suited in solving heat-related high-speed dynamic events [17]. In the discretisation process, difference schemes such as FTCS (Forward Time, Centred Space), Upwind, Lax–Wendroff method are employed to obtain the stable solutions for first and second-order PDEs. Stability and convergence of the solutions are handled using Courant-Friedrichs-Lewy (CFL) [18] and Von Neumann stability analysis [19].

In this work, we introduce finite-difference numerical techniques to develop a thermoelectric model for any given bulk material. Previous researchers (for e.g. [15]) assumed that the temperature dependent properties such as thermal conductivity, electrical conductivity, and Seebeck coefficient of P and N types of a given bulk material are the same. However, as evident from the material information sheet [20], this is not the case. In this work we consider the Seebeck, Peltier, Thomson, and Joule effects, as well as the temperature dependent properties of P and N types of a bulk thermoelectric material separately.

The paper is organized in the following manner. The model is presented with the governing equations, finite-difference formulation and the model configuration in the Numerical Model section. The next section presents a validation of the transient solution of the model by comparing it with the experimental results of Bi_2Te_3 based TEG. It also compared the steady-state solution of the model with the simple 3D finite element ANSYS® simulation for the same material. Results of the model are analysed, studying the voltage distributions in detail. In the final section, the conclusions of our study are presented.

2. Numerical model

The geometry of the model is illustrated in figure 1. Regions 1 and 3 are referred to as the hot-side and the cold-side respectively, and both the regions represent substrate materials (usually electrical insulators: Alumina, Zirconia, Silicon Carbide, etc.). Region 2 represents both P and N thermoelectric materials, combined at either end by an interconnecting material (usually copper). For this work, we neglect this interconnecting material, as it has a negligible impact on the output voltage. As shown in figure 1, the model contains four major boundaries: (1) boundary *A*: the top-most surface at the hot-side which receives constant heat flux from a heat source (2) boundary *B*: the separation surface of the hot-side substrate and thermoelectric materials, (3) boundary *C*: the surface where the cold-side substrate and thermoelectric materials are separated, and (4) boundary *D*: the bottom-most surface at cold-side, which maintains a constant low temperature.

In this section, the model description is described in more detail. Section 2.1 presents the formulation of a set of PDEs that governs thermoelectricity. The explicit finite-difference implementation of the governing differential equations is presented in section 2.2.

2.1. Governing equations

The dynamics of the regions 1 and 3 are governed by the thermal diffusion equation.

$$\frac{\partial T}{\partial t} = \kappa \nabla^2 T \tag{1}$$

$$\kappa = \frac{k}{\rho C_v} \tag{2}$$

where $T(x, \ t)$ is the temperature, κ is the thermal diffusivity of regions 1 and 3, k is the thermal conductivity, ρ is the density, and C_v is the specific heat capacity. Together ρC_v can be considered as the volumetric heat capacity [21]. It is assumed that the above-mentioned material properties are constant within the regions 1 and 3.

The dynamics of the thermoelectric region, region 2, are governed by,

$$\nabla \cdot \left(\frac{\partial D}{\partial t} + J\right) = 0 \tag{3}$$

$$\rho C_v \frac{\partial T}{\partial t} + \nabla \cdot q = Q = J \cdot E \tag{4}$$

where q is the heat flux, J is the electrical current density, $E(x, \ t)$ is the electric field, Q is the internal heat generation rate, and D is the electric flux density. Those thermoelectric governing equations, equations (3) & (4), are coupled by the three constitutive equations: constitutive equation for the electric current, heat flux, and dielectric medium. An in-depth description of these equations can be found in Refs. [22, 23]. Combination of the reversible Seebeck effect and irreversible Joule effect gives the constitutive equation for the electric current.

$$J = \sigma(E - \alpha \nabla T) \tag{5}$$

where σ is the electrical conductivity, and α is the Seebeck coefficient.

Constitutive equation for the heat flux is generated by coupling of the reversible Peltier effect and the irreversible Fourier effect.

$$q = \pi J - k \nabla T \tag{6}$$

where π is the Peltier coefficient. Relation between the Peltier and Seebeck coefficient can be expressed as, $\pi = \alpha T$. Thus, using equation (5) for the electric current J, the constitutive equation for the heat flux becomes,

$$q = \sigma \alpha T E - (k + \sigma \alpha^2 T) \nabla T \tag{7}$$

Constitutive equation for a dielectric medium can be derived from dielectric permittivity ϵ as,

$$D = \epsilon \cdot E \tag{8}$$

Substituting equations (5) (7) (8) into equations (3) (4), thermoelectric governing equations can be rewritten as,

$$\epsilon \frac{\partial E}{\partial t} = -\sigma E + \sigma \alpha \nabla T \tag{9}$$

$$\rho C_v \frac{\partial T}{\partial t} = \sigma(E)^2 - \sigma \alpha E \nabla T + k \nabla^2 T + \sigma \alpha^2 \nabla (T \nabla T) - \sigma \alpha \nabla (T E) \tag{10}$$

In semiconductors, material properties like σ, k, and α usually depend on temperature [24]. The temperature dependency of σ, k, and α results in a material nonlinearity. The involvement of material nonlinearities is a necessity for the precise modelling of thermoelectricity. The temperature dependency of σ, k, and α can be expressed as second-degree polynomial functions.

$$\begin{aligned} \sigma(T) &= \sigma_0 + \sigma_1 T + \sigma_2 T^2 \\ k(T) &= k_0 + k_1 T + k_2 T^2 \\ \alpha(T) &= \alpha_0 + \alpha_1 T + \alpha_2 T^2 \end{aligned} \tag{11}$$

2.2. Finite-difference discretisation

Here, the model structure is utilised as a 1D model, and x-direction is taken as the lengthwise coordinate for A to B, B to C (for both P and N legs), and C to D (see figure 2). Therefore, variations in the electric field and the temperature are assumed to be independent of y- and z-directions. Hence, the 1D equations of equation (1) (9)

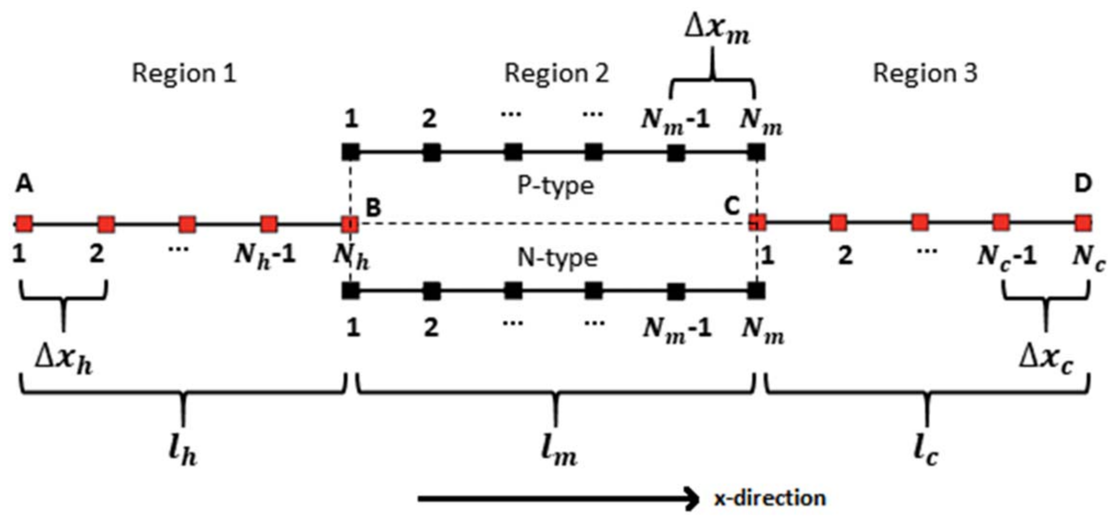

Figure 2. Grid points distribution of 1D FDM TE model. Letters A, B, C, D denotes boundaries A, B, C, D, respectively. l_h and l_c describe the material's length of hot (region 1) and cold (region 3) sides as well l_M is TE material length (region 2). Grid points count of regions 1, 2, 3 is respectively N_h, N_M, N_c. Length between two points is Δx.

and (10) are as follows,

$$\rho C_v \frac{\partial T}{\partial t} = k\frac{\partial^2 T}{\partial x^2} \tag{12}$$

$$\epsilon \frac{\partial E}{\partial t} = -\sigma E + \sigma\alpha \frac{\partial T}{\partial x} \tag{13}$$

$$\rho C_v \frac{\partial T}{\partial t} = \sigma(E)^2 - \sigma\alpha E\frac{\partial T}{\partial x} + k\frac{\partial^2 T}{\partial x^2} + \sigma\alpha^2 \frac{\partial}{\partial x}\left(T\frac{\partial T}{\partial x}\right) - \sigma\alpha\frac{\partial (TE)}{\partial x} \tag{14}$$

The aforementioned governing partial differential equations are discretised using the finite-difference (FD) method. When utilizing the FD method, the spatial domain is first divided into a finite number of points, usually arranged as an evenly dispersed mesh of grid points. Figure 2 illustrates the 1D model structure and grid points distribution throughout the spatial domain. Here we employed FD 'explicit' scheme so that the time domain is explicit. In the explicit scheme, the state of the system at the next time step is calculated from the state of the system at the present time step.

Then the function of x and t, $T(x, \ t)$ and $E(x, \ t)$, are averaged over grid points using differencing schemes. FD method converts linear or non-linear differential equations into a system of linear algebraic equations using these differencing schemes. The solution of each grid point can be obtained by solving those algebraic equations. In this work, we employed Upwind and Lax–Wendroff scheme for solving first-order hyperbolic PDEs and FTCS (forward time, central space) scheme for solving second-order parabolic PDEs. To illustrate the schemes Upwind, Lax–Wendroff and FTCS, consider the following 1D linear hyperbolic first-order PDE (15) and 1D linear parabolic second-order PDE (16) of the form,

$$\frac{\partial U}{\partial t} + \mathrm{A}\frac{\partial U}{\partial x} = 0 \tag{15}$$

$$\frac{\partial U}{\partial t} + \mathrm{A}\frac{\partial^2 U}{\partial x^2} = 0 \tag{16}$$

Applying FD discretisation of spatial and temporal derivatives to equation (15), the Upwind scheme is given by,

$$\frac{U_n^{m+1} - U_n^m}{\Delta t} + \mathrm{A}\frac{U_{n+1}^m - U_n^m}{\Delta x} = 0, \text{ for A} < 0 \tag{17}$$

$$\frac{U_n^{m+1} - U_n^m}{\Delta t} + \mathrm{A}\frac{U_n^m - U_{n-1}^m}{\Delta x} = 0, \text{ for A} > 0 \tag{18}$$

The Lax–Wendroff scheme for solving the PDE (15) is given by,

$$U_n^{m+1} = U_n^m - \Delta t A \frac{U_{n+1}^m - U_{n-1}^m}{2\Delta x} + \frac{1}{2}\Delta t^2 A^2 \frac{U_{n+1}^m - 2U_n^m + U_{n-1}^m}{\Delta x^2} \tag{19}$$

and the FTCS scheme for solving the PDE (16) is given by,

$$\frac{U_n^{m+1} - U_n^m}{\Delta t} = A \frac{U_{n+1}^m - 2U_n^m + U_{n-1}^m}{\Delta x^2} \tag{20}$$

where n is $\mathrm{n_{th}}$ grid point, m is time step counter, $\Delta x = l_{(h,M,c)}/N_{(h,M,c)}$ is the length between two grid points (see figure 2), and $\Delta t = t^{m+1} - t^m$ is the time step.

Hence, expressing the derivatives in terms of respective differencing schemes (using aforementioned schemes), the heat transport in regions 1 and 3 (12) was discretised as,

$$\rho_{(h,c)} C_{v(h,c)} \frac{T_n^{m+1} - T_n^m}{\Delta t} = k_{(h,c)} \frac{T_{n+1}^m - 2T_n^m + T_{n-1}^m}{(\Delta x_{(h,c)})^2} \tag{21}$$

and dynamics of the thermoelectric region (for P- and N-type separately) (13) (14) was discretised as,

$$\begin{aligned} E_n^{m+1} = &\left(1 - \Delta t \frac{\sigma_{(P,N)}}{\epsilon_{(P,N)}}\right) E_n^m + \Delta t \, \frac{\sigma_{(P,N)}\alpha_{(P,N)}}{\epsilon_{(P,N)}} \frac{T_{n+1}^m - T_{n-1}^m}{2\Delta x_{(P,N)}} \\ &+ \frac{1}{2}\Delta t^2 \left(\frac{\sigma_{(P,N)}\alpha_{(P,N)}}{\epsilon_{(P,N)}}\right)^2 \frac{T_{n+1}^m - 2T_n^m + T_{n-1}^m}{(\Delta x_{(h,c)})^2} \end{aligned} \tag{22}$$

$$\begin{aligned} \rho_{(P,N)} C_{v(P,N)} \frac{T_n^{m+1} - T_n^m}{\Delta t} &= \sigma_{(P,N)} (E_n^m)^2 \\ &- \sigma_{(P,N)}\alpha_{(P,N)} E_n^m \frac{T_n^m - T_{n-1}^m}{\Delta x_{(P,N)}} + k_{(P,N)} \frac{T_{n+1}^m - 2T_n^m + T_{n-1}^m}{(\Delta x_{(P,N)})^2} \\ &+ \sigma_{(P,N)}\alpha_{(P,N)}^2 \frac{(T_n^m - T_{n-1}^m)(T_n^m - T_{n-1}^m) + T_n^m(T_{n+1}^m - 2T_n^m + T_{n-1}^m)}{(\Delta x_{(P,N)})^2} \\ &- \sigma_{(P,N)}\alpha_{(P,N)} \frac{(T_n^m - T_{n-1}^m)E_n^m + T_n^m(E_n^m - E_{n-1}^m)}{\Delta x_{(P,N)}} \end{aligned} \tag{23}$$

The model has two boundary equations for the hot and cold surfaces of TEG. When the simulation starts, heat flux $q_A = -k\nabla T$ is imposed at the hot surface (boundary A). Here, $n = 1$ grid point considered as a boundary A (see figure 2), and the temperature at boundary A taken as T_1. Thus, the boundary equation at A can be given as,

$$\rho_{(h)} C_{v(h)} \frac{T_1^{m+1} - T_1^m}{\Delta t} = k_{(h)} \left[\frac{\left(\frac{\partial T}{\partial x}\right)_2^m - \left(\frac{\partial T}{\partial x}\right)_1^m}{\Delta x_{(h)}} \right] \tag{24}$$

If $n = 1 = A$, then the heat flux at $n = 1$ simply assumed as q_A. Hence, the boundary equation at A can be rewritten as,

$$\rho_{(h)} C_{v(h)} \frac{T_1^{m+1} - T_1^m}{\Delta t} = k_{(h)} \left[\Delta \frac{\frac{T_2^m - T_1^m}{\Delta x_{(h)}} + q_A}{\Delta x_{(h)}} \right] \tag{25}$$

Similarly, a constant temperature is maintained near the cold surface (boundary D). Here, $n = N_c$ grid point considered as a boundary D (see figure 2), and the temperature at boundary D taken as T_{N_c}. Therefore, $T_{N_c+1}(=T_{cons})$ point usually considered as a constant temperature value (ambient temperature or temperature of an attached heat sink). Thus, the boundary equation at D can be given as,

$$\rho_{(c)} C_{v(c)} \frac{T_{N_c}^{m+1} - T_{N_c}^m}{\Delta t} = k_{(c)} \frac{T_{cons} - 2T_{N_c}^m + T_{N_c-1}^m}{\Delta(\Delta x_{(c)})^2} \tag{26}$$

In addition, the model uses several boundary equations to calculate the dynamics at boundaries B and C. Here, P and N thermoelectric materials have separate boundary equations. We employed similar techniques proposed in [15] to develop these boundary equations. All the boundary equations are discretised using the aforementioned differencing schemes.

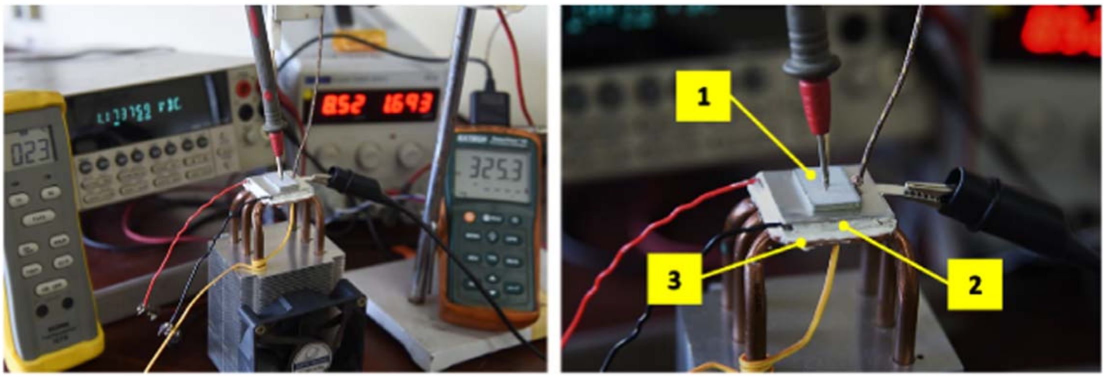

Figure 3. Experimental setup. 1. Hot side PTC heating element 2. Thermoelectric module 3. Cold side heat sink.

Assuming that there is a uniform electric field between two grid points in the model, the potential difference $\Delta\phi$ between two grid points can be expressed as,

$$-\Delta\phi_n = E_n \cdot \Delta x_{(P,\mathrm{N})} \tag{27}$$

The model employed equation (27) in the final stage of calculations to approximate the voltage $V = \sum\phi_n$ across the TE materials.

2.3. Stability and model configuration

The explicit FD method is conditionally stable. Thus, stability criteria need to be satisfied to generate accurate numerical solutions and to stay bound. In this work, Von Neumann stability analysis has been done to verify the stability of second-order parabolic PDEs, as well the Courant-Friedrichs-Lewy (CFL) condition has been used to assure the stability of first-order hyperbolic PDEs. For example, the Von Neumann stability criterion requires the condition

$$r = \frac{\kappa\Delta t}{(\Delta x)^2} \leqslant \frac{1}{2} \tag{28}$$

to be satisfied to ensure the stable behaviour of the numerical solution of the PDE (12), which is second-order parabolic. Similarly, CFL condition ($CFL < 1$) has to be satisfied in hyperbolic PDEs (13) to produce stable numerical solutions. Thus Δt and Δx cannot be chosen arbitrarily. Before starting the computations, our model algorithm first checks the stability criteria of each PDE are satisfied, otherwise it will not allow continuing the calculations if one stability analysis is failed.

Most commercially available TE devices follow the typical 'Sandwich' design, with multiple P and N semiconductor blocks that are arranged electrically in series and thermally in parallel. The TE model developed in this work has been for a single P-N couple of TE materials. Therefore, some scaling has to be done to our TE model to relate the model with the module of multiple P-N couples. The approach for multiple P-N couples can be generalized to the case with a single P-N couple. This way, all the Z number of P-N couples of TEG are lumped into a single P-N couple. This has the effect of scaling transport parameters $\alpha_{tot} = Z\alpha$, $k_{tot} = Zk$, $1/\sigma_{tot} = Z/\sigma$. Thus and so, both transport coefficients in the P and N legs can be considered separately for different materials. This gives the advantage of rejecting the assumptions made in the previous studies such as using equal transport coefficient values for both P and N materials, and replacing transport parameters with their combined values (i.e. $\alpha = \alpha_p - \alpha_n$, $k = k_p + k_n$, $1/\sigma = 1/\sigma_p + 1/\sigma_n$).

Above temperature dependent equations for Bi_2Te_3 were obtained from the information sheet [20].

3. Results and discussion

This section mainly focuses on validating the model through time-dependent transient solutions and steady-state solutions. As a time-dependent test, we compared our model with experimental measurements and the steady state test was compared with a 3D ANSYS® simulation.

3.1. Time-dependent transient solutions

As shown in figures 3 and 4, the experimental setup consists of a PTC ceramic (ceramic with a positive temperature coefficient) heating element, a 3×3 cm commercial TEG, and a heat sink for the cold side. PTC heating element was connected to the hot side to supply a constant heat flux. Heat flux in (25) can be expressed

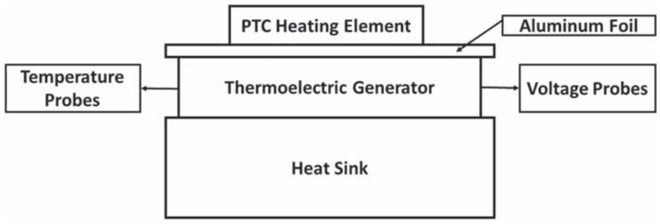

Figure 4. Schematic diagram of experimental setup.

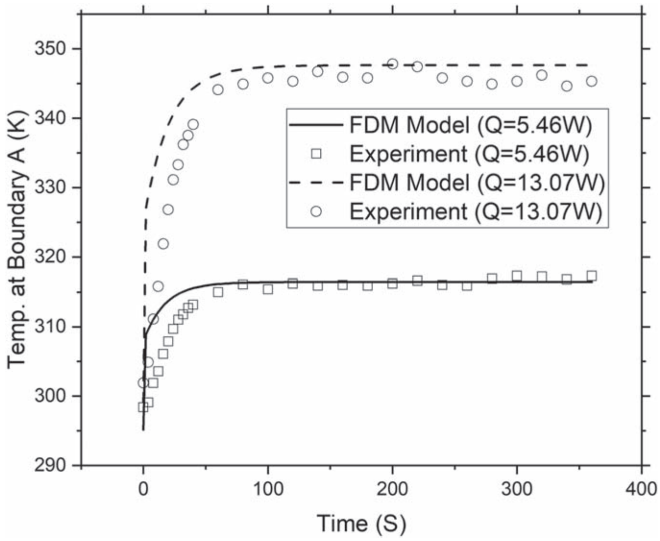

Figure 5. Open-circuit voltage versus time. Lines represent the FDM Model results, and the symbols represent the experimental values.

as, $q_A = Q/A_0$ where Q is the net heat (energy) transfer rate and A_0 is the cross-sectional through which the heat transfer is taking place. In the beginning, the hot surface of the TEG needs to be heated up to get the experimental measurements. Thus, a certain amount of electrical voltage needs to be applied to the PTC heating element. Here we assumed that the electrical power of the PTC heating element was fully converted into thermal energy. A $30 \times 30 \times 0.1$ mm aluminium sheet was used to dissipate the heat energy throughout the top surface of the TEG module, which has 71 P-N couples with bismuth telluride (Bi_2Te_3) based thermoelectric material. On the bottom side, a heat sink with a fan attached was used to maintain a constant temperature at the cold surface of the TEG. Temperature and voltage probes were attached to the experimental setup to get the measurements (see figures 3 and 4). When the experiment initiates, temperature and voltage readings are recorded simultaneously, with time.

Figure 5 shows the experimentally measured open-circuit voltage and calculated open-circuit voltage using the FDM model as a function of time by applying input electrical power of 5.46 W and 13.07 W to the heating element. Throughout the time, the temperature of the cold surface of TEG was maintained at 295.15 K for 5.46 W and 300.15 K for 13.07 W.

Time-dependent open-circuit voltages for the aforementioned two scenarios were obtained from our model by solving the system of discretised PDEs (18) (19) (20) using the C programing language. Transport parameter values for the model were taken from the values listed in table 1. Temperature dependence equations for α, k, σ are also shown beneath table 1. The initial conditions are as follows: 1. The temperature of each grid point (including boundary A and D) was set to 295.15 K for 5.46 W and 300.15 K for 13.07 W, 2. The voltage of each grid point in the thermoelectric region (from B to C) was set to zero. 3. Grid point count = 105 ($N_h = 15$, $N_m = 75$, $N_c = 15$).

According to figure 5, a good agreement can be seen between the 1D finite-difference model and the experimental results. In the beginning, for the two scenarios, the temperatures at the top surface of the TEG (Boundary A) gradually rose from the initial surface temperature to their maximum value due to the heat flux at the boundary A. In 360 seconds, the maximum possible voltage values obtained by the model for two events

Table 1. Thermal and electrical properties of materials [25, 26].

Component	Material	Density ρ (kg m^{-3})	Specific Heat C_v (J kg K^{-1})	Thermal Conductivity k (W mK^{-1})	Electrical Resistivity ρ (Ωm)	Seebeck Coefficient α (V K^{-1})	Dielectric Permittivity ϵ
TEG N leg	Bi_2Te_3	7740	200	a	b	c	290 ⊥
TEG P leg	Bi_2Te_3	7740	200	d	e	f	290 ⊥
Substrate	Ceramic (Alumina)	3220	419	31	N/A	N/A	N/A
PN interconnect	Copper	8300	385	401	1.69×10^{-8}	N/A	N/A

[a] $k_n = (2323000 - 5807T + 6.4681T^2)*10^{-6}$

[b] $\rho_n = (5112 - 163.4T + 0.627T^2)*10^{-8}$

[c] $\alpha_n = (21280 - 1005T + 1.246T^2)*10^{-9}$

[d] $k_p = (7914000 - 35888T + 47.68T^2)*10^{-6}$

[e] $\rho_p = (5112 - 163.4T + 0.627T^2)*10^{-8}$

[f] $\alpha_p = (-234500 + 2123T - 2.541T^2)*10^{-9}$

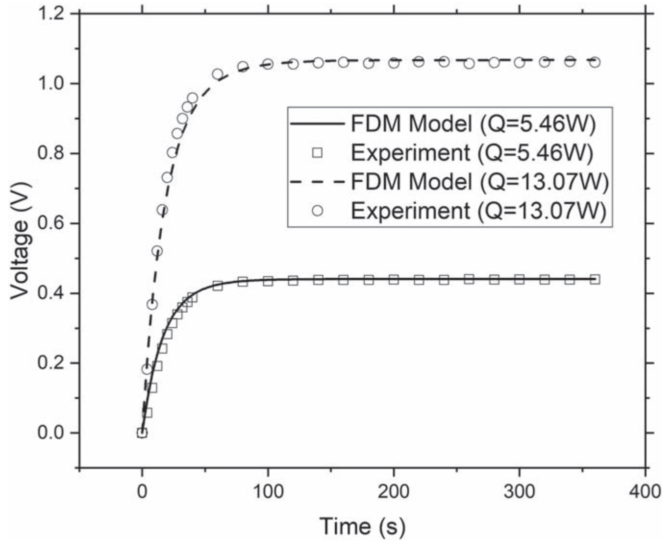

Figure 6. Temperature at the top surface of TEG versus Time. Lines represent the FDM Model results, and the symbols represent the experimental values.

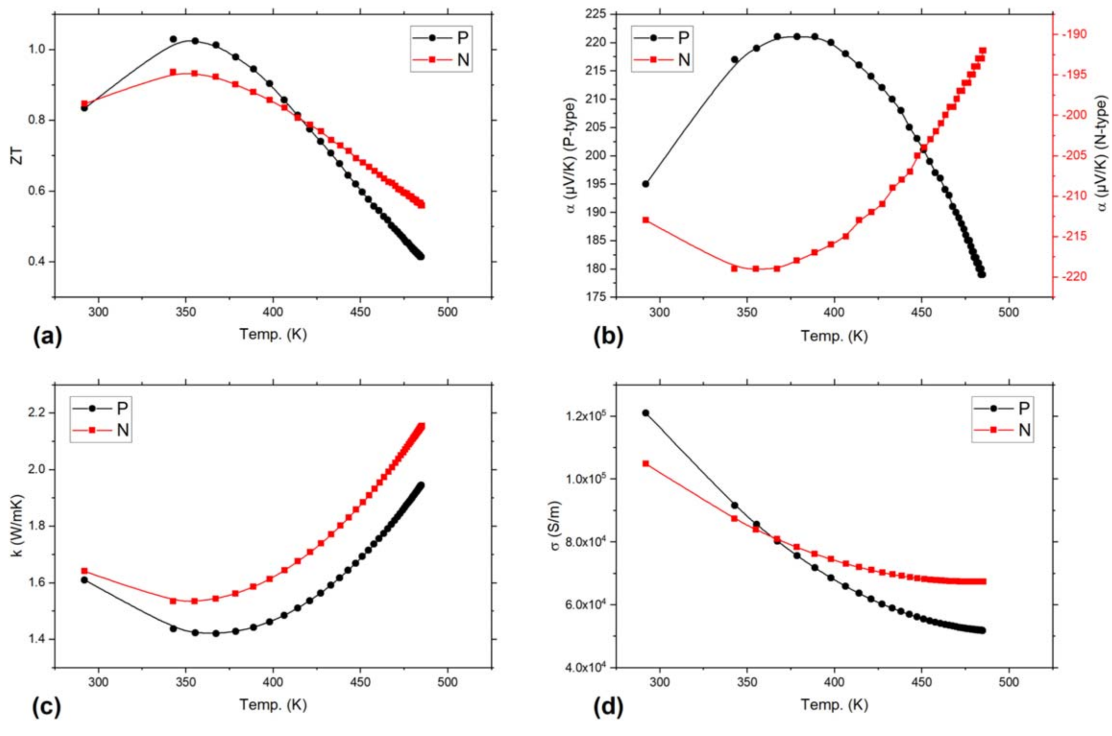

Figure 7. For P-type and N-type thermoelectric material of TEG, (a) dimensionless figure-of-merit, (b) Seebeck coefficient, (c) thermal conductivity, and (d) electrical conductivity versus temperature.

(= 0.441 V for 5.46 W and 1.067 V for 13.07 W) are more consistent with the experimental values (=0.439 V for 5.46 W and 1.061 V for 13.07 W). Figure 6 presents the temperature of Boundary *A* as a function of time. In the early part of both graphs (figures 5, 6), model results slightly deviated from the experiment because the transport parameter coefficients used in the model did come from the literature rather than from experimental values.

Since our FDM model gives promising results in comparison to experimental values, we pushed the model for even higher temperatures to see the temperature-dependent results. Figure 7 shows the temperature-dependent variation of the figure of merit (ZT), Seebeck coefficient, thermal conductivity, and electrical conductivity of both P- and N-type thermoelectric materials of the TEG. For this event, model configurations are as follows: 1. Input power is 59.05 W, 2. The temperature of each grid point was set to 292.15 K, 3. The

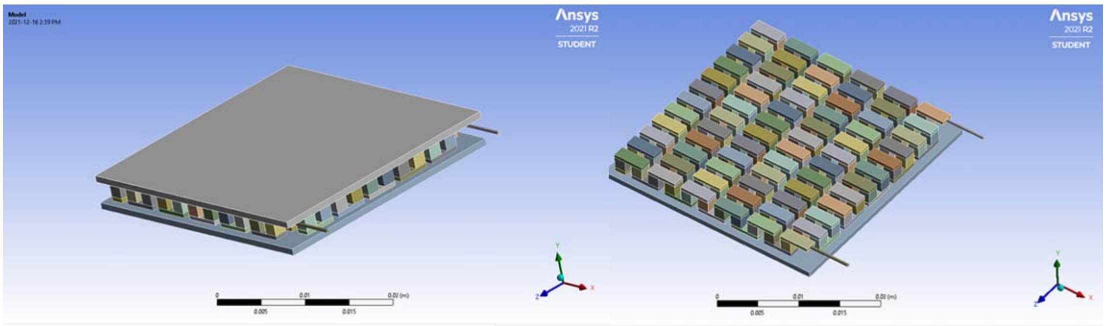

Figure 8. ANSYS® finite-element model.

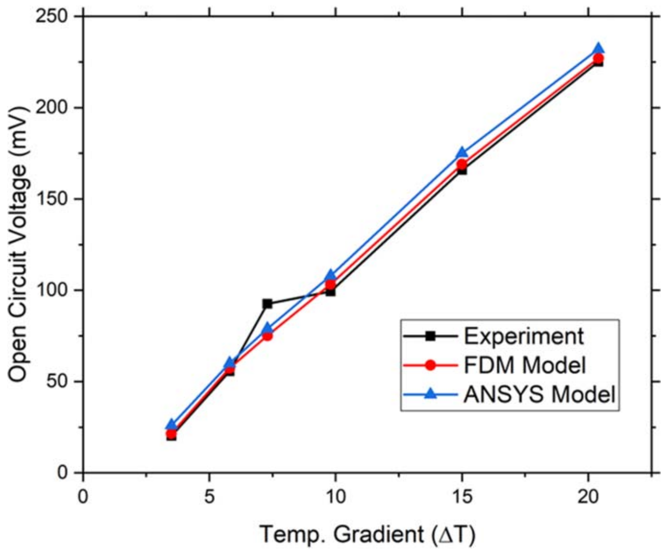

Figure 9. Open circuit voltage versus temperature gradient.

voltage of each grid point in the thermoelectric region was set to zero. 4. Grid point count = 105 ($N_h = 15$, $N_m = 75$, $N_c = 15$).

3.2. Steady-state solutions

As a further test, we developed a 3D finite-element simulation of the thermoelectric model (shown in figure 8) using ANSYS® software to compare the steady-state results of our finite-difference model. This ANSYS® model has the same 71 P-N couples and the same dimensions as the commercial 3×3 cm TEG mentioned in the above section. In the ANSYS® model, the structure of one P-N couple is developed as in figure 1, consist P-N thermoelectric material (Bi2Te3), substrate material (Alumina), and P-N junction interconnect material (Copper). Material properties values from table 1 were used in the ANSYS® model to compute the steady-state results. We computed the solutions for six different temperature gradients using long periods of time and used those values to find steady state voltage values of the FDM model. These values were compared with the direct steady state results from the ANSYS®. Also, we conducted experiments to obtain data related to the particular scenario to ensure the validation. A comparison between the steady-state voltage results of the FDM model, 3D ANSYS® model and the experimental data with several temperature gradients, is shown in figure 9. As shown in the figure, an excellent match among the three methods can be seen, thus validating our approach.

4. Conclusion

In this work, we have developed a finite-difference based one-dimensional model for the thermoelectric device. The governing equations of thermoelectrics were converted into algebraic equations via the finite-difference explicit discretisation technique. In the discretisation process, difference schemes like FTCS, Upwind and Lax–Wendroff method are employed to obtain stable solutions for first and second-order PDEs. The model developed here has several improvements over the existing models. First, the model overcomes the assumptions previously made in the literature like: using equal transport coefficient values for both P and N materials, replacing transport parameters with their combined values. Secondly, the model is time-dependent and considers all the thermal effects (Seebeck, Peltier, Thomson, and Joule), including temperature dependency of properties like thermal conductivity, electrical conductivity, and the Seebeck coefficient. The results of the model have an excellent agreement with the time-dependent experimental values, as well as with the steady-state experimental and ANSYS® 3D simulation results. Therefore, this model can be used to predict the transient and steady-state behaviour of a complete thermoelectric system with multiple P-N elements.

Acknowledgments

Authors wish to acknowledge the financial support offered by the National Research Council of Sri Lanka (Grant No: 15-119).

Data availability statement

The data that support the findings of this study are available upon reasonable request from the authors.

ORCID iDs

R A Rathnayake https://orcid.org/0000-0003-0654-0342
H Wijekoon https://orcid.org/0000-0002-8083-2004
B M K Pemasiri https://orcid.org/0000-0002-1606-3642
N D Subasinghe https://orcid.org/0000-0002-2737-7989

References

[1] Rowe D 1995 *CRC Handbook of Thermoelectrics. Boca Raton* (Florida: CRC Press)
[2] Harb A 2011 Energy harvesting: state-of-the-art *Renewable Energy* **36** 2641–54
[3] Zhang Y, Li J, Hu W, Yang X, Tang X and Tan G 2022 Boosting thermoelectric performance of SnTe by selective alloying and band tuning *Materials Today Energy* **25** 100958
[4] Duong A *et al* 2016 Achieving ZT = 2.2 with Bi-doped n-type SnSe single crystals *Nat. Commun.* **7** 1–6
[5] Liu Z, Cheng H, Le Q, Chen R, Li J and Ouyang J 2022 Giant thermoelectric properties of ionogels with cationic doping *Adv. Energy Mater.* **12** 2200858
[6] Chavez J, Ortega J, Salazar J, Turo A and Garcia M 2000 SPICE model of thermoelectric elements including thermal effects *Proc. IEEE Instrum. Meas. Conf.* **2** 1019–23
[7] Lineykin S and Ben-Yaakov S 2005 Analysis of thermoelectric coolers by a spice-compatible equivalent-circuit model *IEEE Power Electron. Lett.* **3** 63–6
[8] Chen M, Rosendahl L, Bach I, Condra T and Pedersen J 2006 Transient behavior study of thermoelectric generators through an electrothermal model using SPICE *Proc. 25th Int. Conf. Thermoelectrics. 214–219*
[9] Mitrani D, Salazar J, Turó A, García M and Chávez J 2009 One-dimensional modeling of TE devices considering temperature-dependent parameters using SPICE *Microelectron. J.* **40** 1398–405
[10] Antonova E and Looman D 2005 Finite elements for thermoelectric device analysis in ANSYS *24th Int. Conf. Thermoelectrics (ICT). IEEE, 200–203*
[11] Li W *et al* 2015 Multiphysics simulations of a thermoelectric generator *Energy Procedia* **75** 633–8
[12] Jaegle M 2008 Multiphysics simulation of thermoelectric systems - modeling of peltier cooling and thermoelectric generation *Excerpt from the Proc. of the COMSOL Conf. 2008 Hannover*
[13] Sullivan O, Alexandrov B, Mukhopadhyay S and Kumar S 2013 3D compact model of packaged thermoelectric coolers *ASME. J. Electron. Packag.* **135** 031006
[14] Karri M 2011 *Thermoelectric Power Generation System Optimization Studies.* (Potsdam, NY: Clarkson University)
[15] Yan D, Dawson F, Pugh M and El-Deib A 2014 Time-dependent finite-volume model of thermoelectric devices *IEEE Trans. Ind. Appl.* **50** 600–8
[16] Crane D, Koripella C and Jovovic V 2012 Validating steady-state and transient modeling tools for high-power-density thermoelectric generators *J. Electron. Mater.* **41** 1524–34
[17] Momin A A, Shende N, Anamtatmakula A, Ganguly E, Gurbani A, Joshi C A and Mahajan Y Y 2021 *arXiv*)accessed 20-01-2022
[18] Courant R, Friedrichs K and Lewy H 1928 Uber die partiellen Differenzengleichungen der mathematischen Physik *Mathematische Annalen* **100** 32–74
[19] Crank J and Nicolson P 1996 A practical method for numerical evaluation of solutions of partial differential equations of the heat-conduction type *Adv. Comput. Math.* **6** 207–26
[20] Europeanthermodynamics.com.2020 (https://europeanthermodynamics.com/products/datasheets/GM200-71-14-16%20(2).pdf)
[21] United States. Department of the Air Force United States. Department of the Army1988325 Arctic and Subarctic Construction: Calculation Methods for Determination of Depths of Freeze and Thaw in Soils Department of the Army. (https://archive.org/details/ost-military-engineering-tm5_852_6/page/n7/mode/2up)
[22] Ziman J 1960 *Thermoelectrics: Basic Principles and New Material Developments.* (Oxford Clarendon Press)
[23] Chen G 2005 *Nanoscale energy transport and conversion.* (Oxford: Oxford University Press)

[24] Zhang T 2015 Effects of temperature-dependent material properties on temperature variation in a thermoelement *J. Electron. Mater.* **44** 3612–20

[25] Li W *et al* 2017 Multiphysics simulations of thermoelectric generator modules with cold and hot blocks and effects of some factors *Case Studies in Thermal Engineering* **10** 63–72

[26] Madelung O, Rössler U and Schulz M 1998 Non-tetrahedrally bonded elements and binary compounds I. bismuth telluride (Bi2Te3) optical properties, dielectric constant 1-14